NANO LETTERS

Letter

pubs.acs.org/NanoLett

Dependence on Crystal Size of the Nanoscale Chemical Phase Distribution and Fracture in Li_xFePO_4

Young-Sang Yu,[†,‡,§,∥] Chunjoong Kim,[†] David A. Shapiro,[‡] Maryam Farmand,[‡] Danna Qian,[§] Tolek Tyliszczak,[‡] A. L. David Kilcoyne,[‡] Rich Celestre,[‡] Stefano Marchesini,[‡] John Joseph,[⊥] Peter Denes,[‡] Tony Warwick,[‡] Fiona C. Strobridge,[#] Clare P. Grey,[#,▽] Howard Padmore,[‡] Ying Shirley Meng,[§] Robert Kostecki,[∥] and Jordi Cabana*[,†]

[†]Department of Chemistry, University of Illinois at Chicago, Chicago, Illinois 60607, United States

[‡]Advanced Light Source, Lawrence Berkeley National Laboratory, Berkeley, California 94720, United States

[§]Department of NanoEngineering, University of California, San Diego, La Jolla, California 92121, United States

[∥]Energy Storage and Distributed Resources Division, Lawrence Berkeley National Laboratory, Berkeley, California 94720, United States

[⊥]Engineering Division, Lawrence Berkeley National Laboratory, Berkeley, California 94720, United States

[#]Department of Chemistry, University of Cambridge, Lensfield Road, Cambridge CB2 1EW, United Kingdom

[▽]Department of Chemistry, Stony Brook University, Stony Brook, New York 11794, United States

Supporting Information

ABSTRACT: The performance of battery electrode materials is strongly affected by inefficiencies in utilization kinetics and cycle life as well as size effects. Observations of phase transformations in these materials with high chemical and spatial resolution can elucidate the relationship between chemical processes and mechanical degradation. Soft X-ray ptychographic microscopy combined with X-ray absorption spectroscopy and electron microscopy creates a powerful suite of tools that we use to assess the chemical and morphological changes in lithium iron phosphate ($LiFePO_4$) micro- and nanocrystals that occur upon delithiation. All sizes of partly delithiated crystals were found to contain two phases with a complex correlation between crystallographic orientation and phase distribution. However, the lattice mismatch between $LiFePO_4$ and $FePO_4$ led to severe fracturing on microcrystals, whereas no mechanical damage was observed in nanoplates, indicating that mechanics are a principal driver in the outstanding electrode performance of $LiFePO_4$ nanoparticles. These results demonstrate the importance of engineering the active electrode material in next generation electrical energy storage systems, which will achieve theoretical limits of energy density and extended stability. This work establishes soft X-ray ptychographic chemical imaging as an essential tool to build comprehensive relationships between mechanics and chemistry that guide this engineering design.

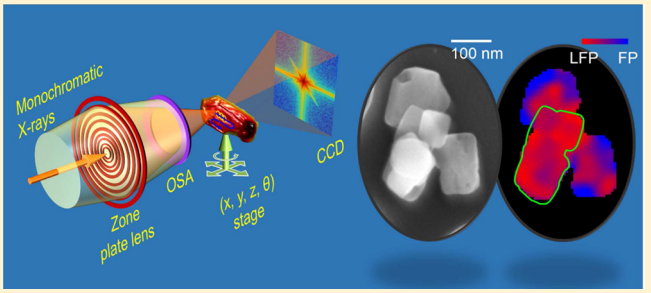

KEYWORDS: *High resolution chemical imaging, battery materials, redox phase transformations, chemo-mechanical coupling, $LiFePO_4$*

Rechargeable Li-ion batteries continue to be at the forefront of electrical energy storage technology with their dominance of the portable electronics market and their incipient development and penetration in large-scale applications such as electric vehicles.[1−3] Yet the remarkable performance of internal combustion engines imposes stringent requirements in battery energy density and life for such applications to become competitive and, thus, widespread. The existing performance limitations can be tracked to slow transport and irreversibilities in the compositional, structural, and morphological changes undergone by the electrode materials during operation, highlighting a general need for an increased fundamental understanding of phase transformations in solids.[4] As a result, tools that provide insight into the onset and propagation of these transitions at high spatial and chemical resolution are critical to identify the mechanisms of electrochemical function, to guide the design of the next generation of materials and architectures for high-energy batteries. This information must be generated at the single particle level, where irreversibilities trigger architecture degradation, and since active electrode materials are used in the form of micro- and even nanopowder form, nanoscale resolution is required. Transmission electron microscopy

Received: January 7, 2015
Revised: May 18, 2015

DOI: 10.1021/acs.nanolett.5b01314
Nano Lett. XXXX, XXX, XXX−XXX

(TEM) combined with electron energy loss spectroscopy (EELS) still offers the highest spatial resolution[5,6] but imposes challenges involving sample thickness and radiation damage,[7] which significantly affect many battery materials.[6,8] A complementary choice is synchrotron-based soft X-ray microscopy coupled with X-ray absorption spectroscopy (XAS), which, for some materials, induces radiation damage at a much lower rate than TEM-EELS.[9] The limitation in spatial resolution of conventional scanning (STXM) and full field (FF TXM) X-ray microscopes has recently been overcome by synchrotron-based soft X-ray ptychographic microscopy, a diffractive imaging method with a demonstrated spatial resolution better than 5 nm.[10]

Since the pioneering work of Padhi et al.,[11] lithium iron phosphate ($LiFePO_4$) has become not only a commercially viable cathode material for safer and environmentally benign lithium-ion batteries[12] but also a model material in the quest to understand phase transformations in the solid state which are driven by a redox process.[13] Its ordered olivine crystal structure with a corner- and edge-sharing polyanion (PO_4^{3-}) host framework offers high capacity at a moderate operation voltage, while giving better chemical and thermal stabilities than layered oxides such as $LiCoO_2$ due to the strong bond between O and both Fe and P ions.[11] Initially, its intrinsic low conductivity[14−16] appeared to limit its viability as an active electrode material. In practice, these issues were overcome through a combination of nanostructuring[17−19] and coatings with electronic[20] and/or ionic[21] conducting layers. The result is that, today, $LiFePO_4$ is one of the best performing materials in the literature, as it is able to sustain reversible capacities close to the theoretical value for many thousands of cycles even at a very high cycle rate.[22] Such fast kinetics prompted interest in its electrochemical (de)lithiation mechanism, which, in equilibrium conditions, involves a first order transition from $LiFePO_4$ to $FePO_4$. Conventionally, such two-phase mechanisms were thought to lead to incomplete and/or irreversible reactions due to kinetic limitations. With the initial proposition of a shrinking core transition within a particle quickly invalidated by the one-dimensional nature of lithium diffusion within $LiFePO_4$,[23−26] other authors reported that phase boundaries mainly between $LiFePO_4$ and $FePO_4$ lie on the *bc* planes and propagate along the *a* axis as the delithiation proceeds, both in micron-[27] and nano-[5,28] sized particles. The dependence on size of the lithium (de)intercalation process in $LiFePO_4$ has long been an object of intense scrutiny in the literature.[13,28−30] The orientation of the phase boundary has been predicted to depend on both the size and morphology of the particle.[31] This behavior has mechanical implications, as strain between the two end members ($LiFePO_4$ and $FePO_4$) is anisotropic in this compound, and particle fracture has been observed upon delithiation.[10,32] It has also been ascertained that when the particles are small, a metastable solid solution pathway exists between $LiFePO_4$ and $FePO_4$ that is followed when the system is under large overpotentials, such as at fast (de)lithiation rates.[13,33,34] The fact that *ex situ* observations of partially delithiated samples by several groups revealed pure $LiFePO_4$ and $FePO_4$ discrete particles[35−37] would be consistent with relaxation from this metastable pathway.

Ultimately, building a comprehensive description of the phase transformation mechanism in $LiFePO_4$ requires imaging techniques capable of resolving chemical components within single nanocrystals. Since $LiFePO_4$ is known to be unstable under electron beams,[6,8] especially in delithiated states, essentially precluding EELS imaging, tools based on X-rays appear as a powerful alternative. Here, we employed soft X-ray ptychographic microscopy combined with XAS[10] to produce high chemical and spatial resolution maps of partially delithiated Li_xFePO_4 single plates of three different sizes. We demonstrate that phases with different oxidation states can now be resolved in crystals as small as ∼100 nm in the longest dimension. Complex distributions of two phases were observed at all crystal sizes. When combining observations from electron and X-ray microscopy, fracture was observed only when the two-phase plates were larger than two hundred nanometers in the longest direction. These two observations identify mechanics as a prominent driver for electrochemical performance.

Li_xFePO_4 powder samples with average composition $x \approx 0.5$, consisting of plates of micrometric (labeled as S-1 hereafter), submicrometric (labeled as S-2 hereafter), and nanometric (labeled as S-3 hereafter) dimensions, were synthesized following hydrothermal[27,39] (S-1 and S-2) and solvothermal[40] (S-3) routes previously reported in the literature and partially delithiated using Br_2 solutions (S-1, S-2, and S-3C). In the case of the nanometric crystals, electrochemical delithiation in a lithium metal half-cell was also conducted (S-3EC). For this purpose, the particles were carbon-coated to maximize activity, prepared into composite electrodes and charged at C/10 against a lithium metal counter electrode until 50% of the total capacity of the cell was accumulated. Additional details may be found in the Supporting Information. The approximate composition was confirmed by XRD (see representative example for S-3C in Figure S2). As shown through a combination of scanning electron microscopy (SEM) and transmission electron microscopy (TEM), the typical particles were elongated, with the large facets measuring, on average, 3.5 × 2.0 μm^2, 1.0 × 0.4 μm^2, and 100 × 80 nm^2 for S-1, S-2, and S-3, respectively (Figures 1 and S3). The average thickness of the plates was roughly 250, 150, and 20 nm for S-1, S-2, and S-3, respectively. Detailed TEM data for partly delithiated micrometric crystals (S-1) are available in earlier publications,[27,32] so only observations for the other two Li_xFePO_4 specimens are discussed here. The Fourier transform of high resolution TEM images revealed that the large facets of both plate-like crystals corresponded to the *ac* plane with the long axis parallel to *c*, in agreement with literature reports.[27,39−41] Extensive fracture was found in a large portion of the S-1 and S-2 particles (Figures 1A,B and S3), with cracks forming roughly parallel to the *c* axis and running internally.[32] In contrast, in an evaluation by TEM of over 100 crystals in S-3C, with sizes ranging between 50 and 200 nm, only one particle was found to show a crack. Representative images of particle ensembles and a high magnification micrograph of the cracked particle are shown in Figure 1C−F. Fracture is the consequence of the accumulation and relaxation of strain due to the mismatch of the $LiFePO_4$ to $FePO_4$ lattice parameters, which involve a 4.9% and 3.5% contraction along the *a* and *b* directions, respectively, and an expansion of 1.9% in the *c* direction, during lithium (de)intercalation.[27,32] The fact that the small partially delithiated particles showed little sign of fracture is consistent with the prediction that the number of potential dislocation sources is severely limited as size is significantly decreased.[42,43]

Soft X-ray ptychographic microscopy,[10] carried out at beamlines 11.0.2 and 5.3.2.1 of the Advanced Light Source, was used to record a series of images of the Li_xFePO_4 crystals across the Fe L_3 absorption edge. Single pixel spectra were produced by integrating the intensity at each energy. Reference

DOI: 10.1021/acs.nanolett.5b01314
Nano Lett. XXXX, XXX, XXX−XXX

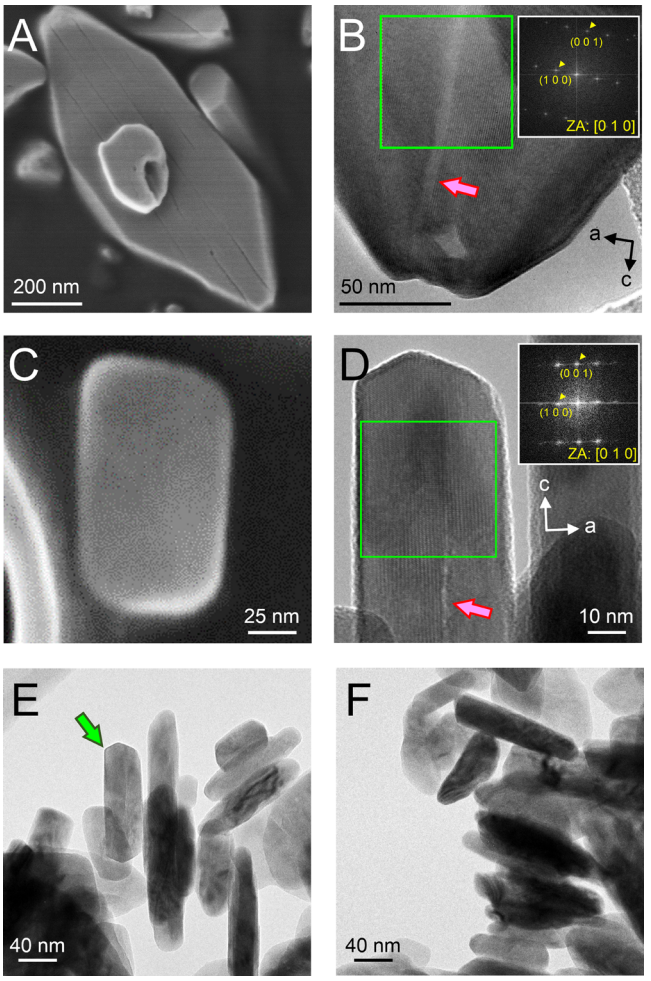

Figure 1. Representative scanning electron microscopy (SEM), together with high resolution transmission electron microscopy (HRTEM) images of Li_xFePO_4 (A,B) S-2 and (C,D) S-3C. A representative SEM image for S-1 is shown in Figure S3. The insets in B and D show the Fourier transformation patterns produced from the regions marked by the green box, indicating the crystallographic orientation of the crystals and the [010] zone axis for these HRTEM images. Defects are indicated by the red arrows in HRTEM images (B,D). (E,F) Transmission electron microscopy (TEM) images of a larger collection of S-3C nanocrystals. The cracked particle shown in D is indicated by the green arrow in E. The crack is clearly detected even in this low magnification image.

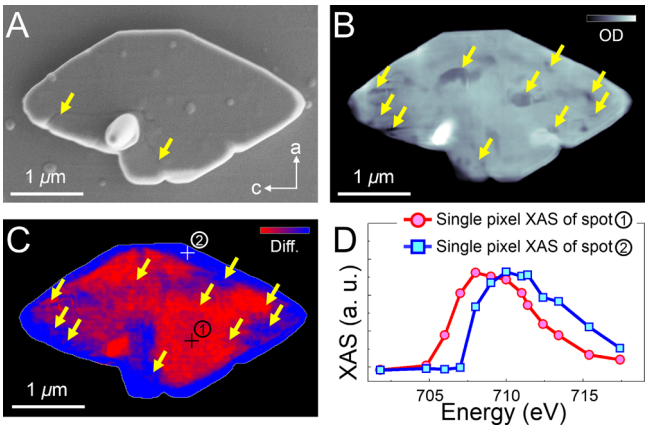

Figure 2. (A) Scanning electron microscopy (SEM) image and (B) optical density (OD) map obtained by ptychographic microscopy of a crystal in sample S-1. To enhance the mass thickness contrast, three OD maps collected at the pre-edge region (two images at 701.8 and one image at 704.8 eV) were averaged. The darker areas in the crystals (indicated by yellow arrows) indicate regions of lower density, which occur as expected near the surface but are also present due to internal defects (cracks and voids). (C) Difference map between ptychographic microscopy images collected at 708 and 710 eV. To eliminate differences in mass thickness contrast, both images were normalized by the image at 701.8 eV. The red and blue areas indicate the highest content of $LiFePO_4$ and $FePO_4$, respectively. Defect positions, which are confirmed by the OD map in (B), are also identified by yellow arrows. (D) Selected single pixel XAS from spots 1 and 2 in C. The XAS intensity is saturated near 708 and 710 eV owing to the thickness of the sample.

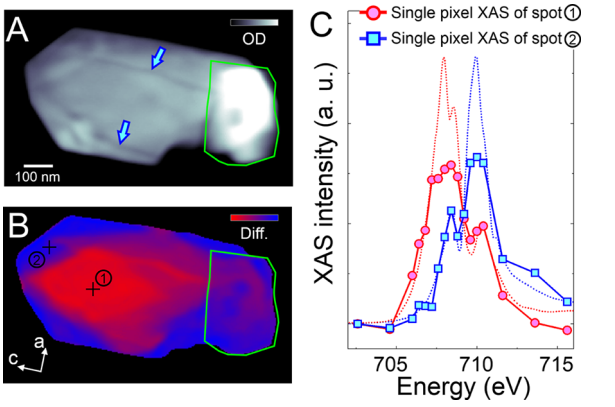

Figure 3. (A) Optical density (OD) map of a selected crystal in S-2 collected at 709.2 eV using a ptychographic reconstruction. To minimize the contrast difference due to the chemical composition, the optical density map was collected at the nearest energy point to the isosbestic point (see Figure S4). The darker areas in the crystals indicate regions of lower density, as expected near the cracks, pointed out by blue arrows. (B) Difference map between OD maps at 708 and 710 eV. To eliminate mass thickness contrast, both OD images were normalized by an image collected at 700 eV. The red and blue areas indicate the highest content of $LiFePO_4$ and $FePO_4$, respectively. The regions outlined green in A and B indicate areas of particle overlap, determined by the morphological optical density image at 710 eV. (C) Selected single pixel XAS from spots 1 and 2 in B with $FePO_4$ (blue dashed line) and $LiFePO_4$ (red dashed line) standard spectra. The XAS intensity is saturated near 708 and 710 eV owing to the excessive absorption through the thickness of the sample.

spectra for pristine $LiFePO_4$ and chemically delithiated $FePO_4$ crystals were extracted from linescans with an energy step of 0.2 eV (see Supporting Information and Figure S4 for details). Figures 2–4 and 6 show the chemical phase distributions for the four different types of Li_xFePO_4 crystal. Consistent with previous reports,[36] $FePO_4$ (Fe^{3+}) is characterized by an Fe L_3 edge with a peak maximum near 710 eV, whereas $LiFePO_4$ (Fe^{2+}) has a maximum peak intensity near 708 eV. Morphological information was extracted from the ptychographic microscopy images at the pre-edge region (Figure 2) or the closest energy point to the isosbestic point (709.15 eV obtained from the reference spectra, Figures 3, 4, and 6), where the contrast difference due to the chemical composition is minimized.

The images in Figure 2A–C correspond to the same micrometric Li_xFePO_4 crystal (S-1), imaged by SEM and ptychographic microscopy. The SEM image revealed a few cracks, indicated by the yellow arrows in Figure 2A. Since the SEM images were collected by low dose mode with very low

DOI: 10.1021/acs.nanolett.5b01314
Nano Lett. XXXX, XXX, XXX–XXX

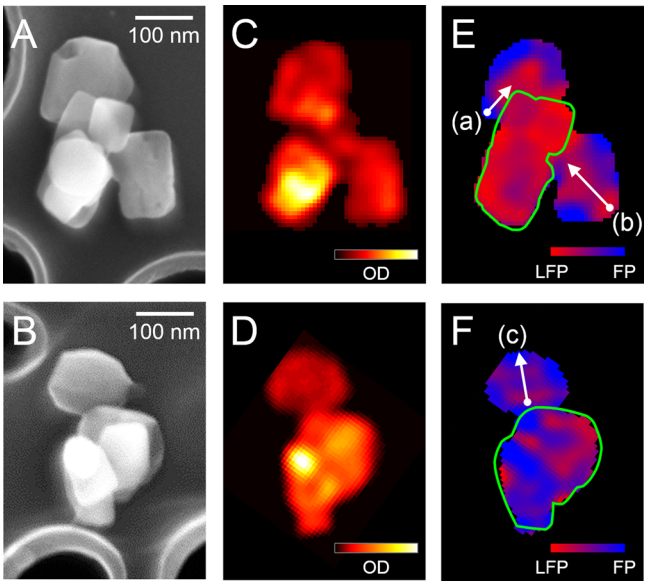

Figure 4. (A,B) Scanning electron microscope (SEM) images of selected crystals in S-3C. (C,D) Optical density (OD) maps reconstructed by ptychographic microscopy. To minimize the contrast difference due to the chemical composition, the OD map was collected at the nearest energy point (C, 709.2 eV; D, 709.1 eV) to the isosbestic point. (E,F) Chemical phase maps obtained by linear combination fits of XAS data at each pixel. The presence of the $LiFePO_4$ (LFP) and $FePO_4$ (FP) were assigned colors red and blue, respectively. The regions outlined green indicate areas of particle overlap, identified by SEM.

accelerating voltage (1 kV) to prevent charge build-up, only surface features were observed. In contrast, the intensity (brightness) in the optical density (OD) image (Figure 2B) collected by ptychographic microscopy in transmission mode is directly proportional to the mass through the thickness of the crystal. Therefore, the dark features in the OD image were ascribed to microstructural defects (cracks or voids) both at the surface and, in particular, inside the crystal as indicated by the yellow arrows in Figure 2B. Both the surface and internal cracks showed a general tendency toward being oriented along the *c* direction. To study the correlation between the morphological defects and the chemical phase distribution, a difference map was generated between the OD images collected at 708 and 710 eV, normalized by the image at 701.8 eV to eliminate the mass thickness contrast (Figure 2C). The spectra from single pixels at the center and edge of the particle (Figure 2D) showed highly distorted features near the main absorption peaks of $LiFePO_4$ (708 eV) and $FePO_4$ (710 eV) due to saturation, thereby precluding quantitative analysis. However, qualitatively, the intensity differences at 708 and 710 eV were still found to provide chemical contrast between $LiFePO_4$-rich and $FePO_4$-rich domains. Therefore, the red and blue colored areas in the difference map indicate the highest content of $LiFePO_4$ and $FePO_4$, respectively. Results obtained by principal component analysis (PCA) of the data and subsequent *k*-means clustering[32,44] were in excellent agreement with the chemical phase distribution collected from the OD difference map (see Supporting Information for details and Figure S5). The results closely resembled previous data collected by a combination of STXM and FF TXM.[32] Delithiation occurred extensively around the edges of the crystal, but it was uneven and lacked clear directionality. Reacted domains were also scattered within the center of the crystal. Nonetheless, a trend toward correlation of these reacted domains with the most obvious cracks was observed, especially on the left-hand side of the particle as it is shown. The penetration of delithiated domains laterally into the particle follows the pattern of fracture in the optical density map (see arrows for guides to the eye in Figure 2).

Similar analyses were previously performed for the partially delithiated submicrometric crystals (S-2).[10] They are shown again in Figure 3 for completeness. For consistency, we focus now only on the absorption contrast rather than the full complex contrast, which is available by ptychographic imaging. The OD image revealed a few cracks, which are roughly oriented along the *c*-direction, indicated by the blue arrows in Figure 3A. Despite the reduced thickness compared to S-1, the absorption spectra from single pixels at the center and edge of the particle still showed signs of saturation near 708 and 710 eV (Figure 3C). The OD difference map between 708 and 710 eV clearly revealed a distribution of $LiFePO_4$-rich and $FePO_4$-rich regions, as indicated again in red and blue, respectively (Figure 3B). PCA results show excellent agreement with the OD difference map (Figure S6). Note that Figure 3A,B shows an elongated hexagonal plate with an overlapping particle on it, indicated by the green outlined region. The chemical phase distribution in the S-2 crystal was complex and very similar to the maps collected from much larger plates (S-1, Figure 2). The delithiated domains located along the outer areas led to an apparent diamond-like pattern of central lithium rich domains, yet the phase boundary between two chemical phases did not proceed straight from the short particle edges or their adjacent corners. In addition, the chemical domains were not symmetric along either *a* or *c* direction, yielding a highly irregular diamond-like pattern. Thus, as for S-1, a clear crystallographic direction for the phase propagation could not be established. In contrast, correspondence between the formation of cracks (Figures 2B and 3A) roughly along the *c* direction and the phase transformation reaction (Figures 2C and 3B) was very apparent. Fe XAS intensity, while lower than the rest of the crystal before normalization, was still observed in the crack region. Therefore, fracture did not propagate vertically (i.e., along the *b* direction) throughout the whole crystal, as this situation would create a material void in the crystal, leading to complete Fe signal loss. Furthermore, as already discussed in our previous report,[10] in some areas, significant delithiation was found to occur on both sides of each crack, but not within the crack itself, indicative of a reaction limited by solid state diffusion. The new high resolution setup enables the elucidation of the correlation between mechanics and chemistry, not possible in prior lower resolution work.[32]

Chemical phase maps for S-3C are illustrated in Figure 4. Particles of interest were identified by low resolution STXM and SEM over a large area (over 250 crystals were studied). High resolution ptychographic microscopy was performed only on the best candidates, as defined by their degree of overlap. All single pixel spectra were fit by a linear combination (LC) of standard spectra (Figure S4) of $LiFePO_4$ and $FePO_4$. Pixels showing poor signal-to-noise ratios were filtered out by a lower bound of the *R*-factor.[32,45] Representative single pixel XAS and the corresponding fits are presented in Figure S7. The accuracy of the LC fit is represented by *R*-factor maps in Figure S8. Around 94% of pixels (94.59% for Figure 4E and 94.48% for Figure 4F) were fit with *R*-factors less than 0.05. The presence of $LiFePO_4$ and $FePO_4$ in a given pixel resulting from the fits

DOI: 10.1021/acs.nanolett.5b01314
Nano Lett. XXXX, XXX, XXX−XXX

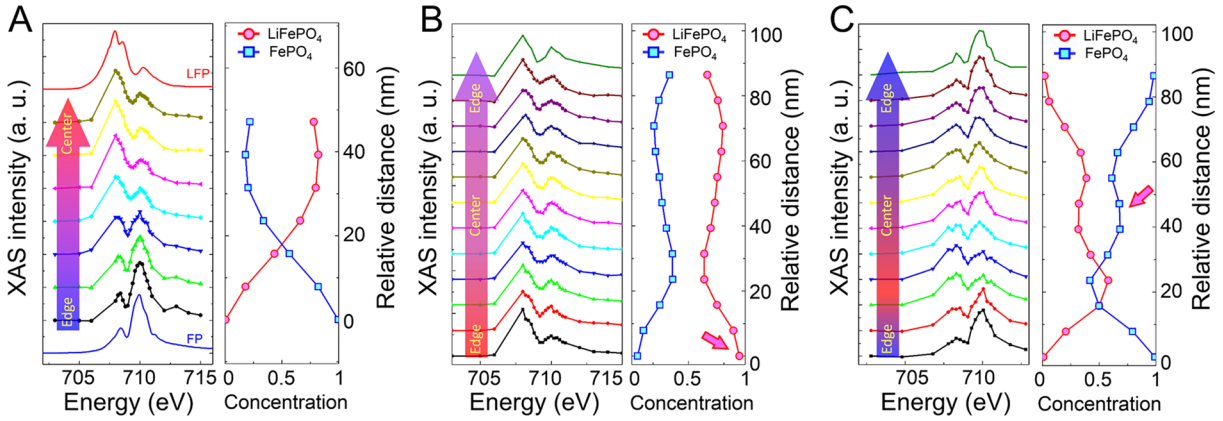

Figure 5. Fe L_3 X-ray absorption spectra collected along the paths defined by (a), (b), and (c) in Figure 4 (A, B, and C, respectively). Reference spectra (solid red and blue lines in A) taken for pristine $LiFePO_4$ and chemically delithiated $FePO_4$ are also shown for comparison. Chemical concentration profiles of $LiFePO_4$ and $FePO_4$ obtained by linear combination fits of the spectra at each path and the relative positions are presented in the adjacent panels.

are represented by red and blue, respectively. In order to aid the interpretation of the complex images, chemical maps were also produced which visualize the contents of a single standard (Figure S9). The averaged XAS from the entirety of each nonoverlapped particle revealed an average composition Li_xFePO_4 with x = 0.48 (upper left side particle in Figure 4E), 0.53 (lower right side particle in Figure 4E), and 0.31 (Figure 4F). The details of the average spectra are presented in Figure S10. These measured composition variations between the particles indicate that kinetic factors determine the ultimate phase ratio in the individual crystals.

Single crystals composed of both $LiFePO_4$ and $FePO_4$ could be clearly identified in S-3C. This result is in agreement with data from Laffont et al.[5] and Wagemaker et al.,[46] who prepared Li_xFePO_4 following similar methods. From previous reports, the phase boundaries are expected to strongly correlate with crystallographic orientation[5,27,41,47] because chemical interfacial and coherency strain energy have different anisotropies.[31] The distribution in the S-3C nanoplate was complex and irregular, without a clear crystallographic directionality. As in the case of the larger plates, delithiation appeared to be more extensive at the crystal edges. Yet, unlike the larger plates, no surface and internal cracks that could kinetically control phase propagation were observed by SEM (Figures 1C and 4A,B), TEM (Figure 1E,F), and the transmission X-ray images (Figure 4C,D). Furthermore, a significant amount of $LiFePO_4$ was found on the edge of some crystals (see red arrows in Figure 5B) and $FePO_4$-rich sites were also detected at the center (see red arrow in Figure 5C). In transmission geometry, mixed compositions reflect incomplete delithiation along the direction of the X-ray beam. Unlike previous studies,[37] single nanoparticles were found that were not fully transformed and had many interfacial domains, as shown in Figures 4 and 5. This observation indicates that multiple nucleation sites existed for the formation of $FePO_4$ in these conditions.[48]

Literature reports indicate that only the smallest plates can be effectively delithiated in an electrochemical cell;[49] the response of the latter sample is shown in Figure S1. Crystals recovered from one such cell at 50% average state-of-charge (sample S-3EC, Figure 6) were imaged and compared to S-3C. Particle overlap was ascertained from the intensity of the optical density at each pixel (Figure 6A,B). The trends observed were generally the same. First, crystals were located where $LiFePO_4$

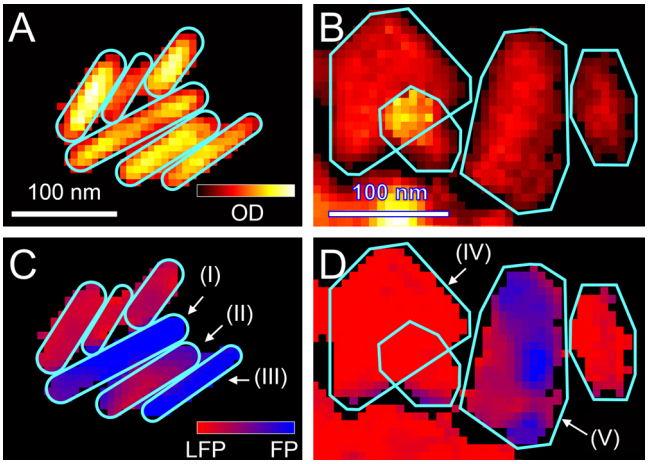

Figure 6. (A,B) Optical density (OD) maps of selected crystals in S-3EC reconstructed by ptychographic microscopy. To minimize the contrast difference due to the chemical composition, the OD map was collected at the nearest energy point (709 eV) to the isosbestic point. (C,D) Chemical phase maps obtained by linear combination fits of XAS data at each pixel. The presence of the $LiFePO_4$ (LFP) and $FePO_4$ (FP) were assigned colors red and blue, respectively. The regions outlined cyan indicate areas where isolated single particles exist.

and $FePO_4$ coexisted (see crystals II and V in Figure 6C and D, respectively). Second, delithiation in crystals with mixed composition was more prominent at particle edges (see crystals II and V in Figure 6C and D, respectively), yet without a clear pattern of distribution. Third, the levels of delithiation were rather inhomogeneous, as crystals containing high concentrations of either $FePO_4$ (see crystals I and III in Figure 6C) and $LiFePO_4$ (see crystal IV in Figure 6D) could also be observed in the same sample. Finally, no morphological defects were apparent in the optical density images (Figure 6A,B). All in all, the similarity between both preparation methods is indicative of the validity of chemical delithiation to study these battery reactions, at least under the conditions employed here.

It is typically assumed that, during first order transitions such as $LiFePO_4$–$FePO_4$, there is a negligible driving force for equilibration when the redox stimulus (oxidizing agent or current) is removed,[50] or that, at least, interface orientation is maintained during relaxation.[47] However, a metastable pathway

DOI: 10.1021/acs.nanolett.5b01314
Nano Lett. XXXX, XXX, XXX−XXX

involving continuous miscibility between $LiFePO_4$ and $FePO_4$ exists for nanoparticles when the reaction occurs at high rates.[29,33,34] This mechanism is activated by the large surface energy penalty for the formation of a phase boundary within such small crystals, with the reaction overpotential providing the driving force.[29] When the electrochemical stimulus is removed, metastable solid solutions equilibrate to the thermodynamically favored two-phase separation. However, due to the unfavorable formation of boundaries within a particle when it is very small,[29,51] such separation involves interparticle exchange of Li,[38] so that the end result is a mixture of particles that are composed of either pure $LiFePO_4$ or pure $FePO_4$.[37] Such relaxation is unlikely to explain the observations made for the smallest crystals in this study, consistent with the slow rate used in the cell to produce S-3EC. Moreover, interparticle exchange cannot occur in chemically delithiated samples because the reaction medium is poorly conducting of both ions and electrons, required for such exchange.

Although the distribution of chemical phases was found to be almost identical among micron-,[32,52] submicron-,[10] and nano-sized $LiFePO_4$ plates, the electrochemical performance is strongly dependent on their size.[49] Such performance is closely correlated with fatigue at the electrodes, which can be induced by the fracture of the particle.[53] It is clear from the data presented here that phase coexistence can be accommodated without fracture in small particles. In cycling conditions where such coexistence may exist, such as slow rates, failure due to strain will be less likely if the particles are small. While the reduction of particle size to accommodate strain has long been sought as an enabler of high capacity battery materials such as Si,[54] mechanics have received less attention in intercalation materials such as $LiFePO_4$ due to the smaller volume changes compared to alloy-based electrodes. Generally, nanoscaling in this context is proposed so as to shorten solid state diffusion lengths and increase electrode−electrolyte interfaces.[55] Our work reinforces the importance of mechanical considerations to optimize the electrochemical performance of $LiFePO_4$ and, likely, other materials undergoing first order transitions.[56] Establishing the specific chemo-mechanics correlations would require making these high resolution observations during the reaction. It could provide novel and important clues into what crystal dimensionality is needed for the best electrochemical properties, as well as experimental validation by theories of nonequilibrium solid solution mechanisms.[29,34]

■ ASSOCIATED CONTENT

Ⓢ Supporting Information

Materials and methods, and data analysis. The Supporting Information is available free of charge on the ACS Publications website at DOI: 10.1021/acs.nanolett.5b01314.

■ AUTHOR INFORMATION

Corresponding Author

*E-mail: jcabana@uic.edu.

Author Contributions

Y.-S.Y., C.K., Y.S.M., R.K., C.P.G., D.A.S., and J.C. conceived and planned the experiment. D.A.S., T.T., A.L.D.K., A.S., T.W., Y.-S.Y., and H.P. developed experimental techniques, software, and equipment. D.A.S. and S.M. developed data processing and ptychographic microscopy reconstruction codes. Y.-S.Y., C.K., F.C.S., and C.P.G. prepared the samples. Y.-S.Y., M.F., and D.A.S. carried out the ptychographic microscopy measurements. Y.-S.Y. and D.A.S. performed postexperiment data analysis, and Y.-S.Y., C.K., and J.C. established the interpretation of the chemical maps. D.Q., Y.-S.Y., C.K., and Y.S.M. carried out the TEM measurements and imaging analysis. Y.-S.Y., C.K., D.A.S., and J.C. prepared the manuscript, which incorporates critical input from all authors.

Notes

The authors declare no competing financial interest.

■ ACKNOWLEDGMENTS

This work was supported as part of the NorthEast Center for Chemical Energy Storage, an Energy Frontier Research Center funded by the U.S. Department of Energy, Office of Science, Office of Basic Energy Sciences under Award Number DE-SC0012583. Soft X-ray ptychographic microscope works were carried out at either beamline 11.0.2 or beamline 5.3.2.1 at the Advanced Light Source. The Advanced Light Source is supported by the Director, Office of Science, Office of Basic Energy Sciences, of the U.S. Department of Energy under Contract No. DE-AC02-05CH11231. The TEM experiments were carried out through a user project supported by Center for Nanophase Materials Sciences (CNMS) at Oak Ridge National Laboratory, which is sponsored by the Scientific User Facilities Division, Office of Basic Energy Sciences, U.S. Department of Energy. This work is partially supported by the Center for Applied Mathematics for Energy Research Applications (CAMERA), which is a partnership between Basic Energy Sciences (BES) and Advanced Scientific Computing Research (ASRC) at the U.S. Department of Energy. The authors wish to thank Dr. Guoying Chen (LBNL) for providing samples used in this manuscript.

■ REFERENCES

(1) Armand, M.; Tarascon, J. M. *Nature* **2008**, *451* (7179), 652−657.
(2) Wu, C. *MRS Bull.* **2010**, *35* (9), 650−651.
(3) Goodenough, J. B.; Kim, Y. *Chem. Mater.* **2009**, *22* (3), 587−603.
(4) Van der Ven, A.; Bhattacharya, J.; Belak, A. A. *Acc. Chem. Res.* **2012**, *46* (5), 1216−1225.
(5) Laffont, L.; Delacourt, C.; Gibot, P.; Wu, M. Y.; Kooyman, P.; Masquelier, C.; Tarascon, J. M. *Chem. Mater.* **2006**, *18* (23), 5520−5529.
(6) Moreau, P.; Mauchamp, V.; Pailloux, F.; Boucher, F. *Appl. Phys. Lett.* **2009**, *94* (12), 123111.
(7) Hitchcock, A. P.; Dynes, J. J.; Johansson, G.; Wang, J.; Botton, G. *Micron* **2008**, *39* (3), 311−319.
(8) Pan, Y.-H.; Vaughan, G.; Brydson, R.; Bleloch, A.; Gass, M.; Sader, K.; Brown, A. *Ultramicroscopy* **2010**, *110* (8), 1020−1032.
(9) Rightor, E. G.; Hitchcock, A. P.; Ade, H.; Leapman, R. D.; Urquhart, S. G.; Smith, A. P.; Mitchell, G.; Fischer, D.; Shin, H. J.; Warwick, T. *J. Phys. Chem. B* **1997**, *101* (11), 1950−1960.
(10) Shapiro, D. A.; Yu, Y.-S.; Tyliszczak, T.; Cabana, J.; Celestre, R.; Chao, W.; Kaznatcheev, K.; Kilcoyne, A. L. D.; Maia, F.; Marchesini, S.; Meng, Y. S.; Warwick, T.; Yang, L. L.; Padmore, H. A. *Nat. Photon.* **2014**, *8*, 765−769.
(11) Padhi, A. K.; Nanjundaswamy, K. S.; Goodenough, J. B. *J. Electrochem. Soc.* **1997**, *144* (4), 1188−1194.
(12) Zaghib, K.; Mauger, A.; Julien, C. M. *J. Solid State Electrochem.* **2012**, *16* (3), 835−845.
(13) Malik, R.; Abdellahi, A.; Ceder, G. *J. Electrochem. Soc.* **2013**, *160* (5), A3179−A3197.
(14) Delacourt, C.; Laffont, L.; Bouchet, R.; Wurm, C.; Leriche, J.-B.; Morcrette, M.; Tarascon, J.-M.; Masquelier, C. *J. Electrochem. Soc.* **2005**, *152* (5), A913−A921.
(15) Chung, S.-Y.; Bloking, J. T.; Chiang, Y.-M. *Nat. Mater.* **2002**, *1* (2), 123−128.

DOI: 10.1021/acs.nanolett.5b01314
Nano Lett. XXXX, XXX, XXX−XXX

(16) Tang, X.-C.; Li, L.-X.; Lai, Q.-L.; Song, X.-W.; Jiang, L.-H. *Electrochim. Acta* **2009**, *54* (8), 2329−2334.
(17) Delacourt, C.; Poizot, P.; Levasseur, S.; Masquelier, C. *Electrochem. Solid-State Lett.* **2006**, *9* (7), A352−A355.
(18) Yamada, A.; Chung, S. C.; Hinokuma, K. *J. Electrochem. Soc.* **2001**, *148* (3), A224−A229.
(19) Huang, H.; Yin, S.-C.; Nazar, L. F. *Electrochem. Solid-State Lett.* **2001**, *4* (10), A170−A172.
(20) Ravet, N.; Chouinard, Y.; Magnan, J. F.; Besner, S.; Gauthier, M.; Armand, M. *J. Power Sources* **2001**, *97*−*98*, 503−507.
(21) Kang, B.; Ceder, G. *Nature* **2009**, *458* (7235), 190−193.
(22) Zaghib, K.; Dontigny, M.; Guerfi, A.; Charest, P.; Rodrigues, I.; Mauger, A.; Julien, C. M. *J. Power Sources* **2011**, *196* (8), 3949−3954.
(23) Islam, M. S.; Driscoll, D. J.; Fisher, C. A. J.; Slater, P. R. *Chem. Mater.* **2005**, *17* (20), 5085−5092.
(24) Morgan, D.; Van der Ven, A.; Ceder, G. *Electrochem. Solid-State Lett.* **2004**, *7* (2), A30−A32.
(25) Nishimura, S.-I.; Kobayashi, G.; Ohoyama, K.; Kanno, R.; Yashima, M.; Yamada, A. *Nat. Mater.* **2008**, *7* (9), 707−711.
(26) Malik, R.; Burch, D.; Bazant, M.; Ceder, G. *Nano Lett.* **2010**, *10* (10), 4123−4127.
(27) Chen, G.; Song, X.; Richardson, T. J. *Electrochem. Solid-State Lett.* **2006**, *9* (6), A295−A298.
(28) Yamada, A.; Koizumi, H.; Nishimura, S.-i.; Sonoyama, N.; Kanno, R.; Yonemura, M.; Nakamura, T.; Kobayashi, Y. *Nat. Mater.* **2006**, *5* (5), 357−360.
(29) Malik, R.; Zhou, F.; Ceder, G. *Nat. Mater.* **2011**, *10* (8), 587−590.
(30) Kobayashi, G.; Nishimura, S.-i.; Park, M.-S.; Kanno, R.; Yashima, M.; Ida, T.; Yamada, A. *Adv. Funct. Mater.* **2009**, *19* (3), 395−403.
(31) Abdellahi, A.; Akyildiz, O.; Malik, R.; Thornton, K.; Ceder, G. *J. Mater. Chem. A* **2014**, *2* (37), 15437−15447.
(32) Boesenberg, U.; Meirer, F.; Liu, Y.; Shukla, A. K.; Dell'Anna, R.; Tyliszczak, T.; Chen, G.; Andrews, J. C.; Richardson, T. J.; Kostecki, R.; Cabana, J. *Chem. Mater.* **2013**, *25* (9), 1664−1672.
(33) Zhang, X.; van Hulzen, M.; Singh, D. P.; Brownrigg, A.; Wright, J. P.; van Dijk, N. H.; Wagemaker, M. *Nano Lett.* **2014**, *14* (5), 2279−2285.
(34) Liu, H.; Strobridge, F. C.; Borkiewicz, O. J.; Wiaderek, K. M.; Chapman, K. W.; Chupas, P. J.; Grey, C. P. *Science* **2014**, *344* (6191), 1252817.
(35) Li, Y.; El Gabaly, F.; Ferguson, T. R.; Smith, R. B.; Bartelt, N. C.; Sugar, J. D.; Fenton, K. R.; Cogswell, D. A.; Kilcoyne, A. L. D.; Tyliszczak, T.; Bazant, M. Z.; Chueh, W. C. *Nat. Mater.* **2014**, *13* (12), 1149−1156.
(36) Chueh, W. C.; El Gabaly, F.; Sugar, J. D.; Bartelt, N. C.; McDaniel, A. H.; Fenton, K. R.; Zavadil, K. R.; Tyliszczak, T.; Lai, W.; McCarty, K. F. *Nano Lett.* **2013**, *13* (3), 866−872.
(37) Delmas, C.; Maccario, M.; Croguennec, L.; Le Cras, F.; Weill, F. *Nat. Mater.* **2008**, *7* (8), 665−671.
(38) Dreyer, W.; Jamnik, J.; Guhlke, C.; Huth, R.; Moskon, J.; Gaberscek, M. *Nat. Mater.* **2010**, *9* (5), 448−453.
(39) Dokko, K.; Koizumi, S.; Nakano, H.; Kanamura, K. *J. Mater. Chem.* **2007**, *17* (45), 4803−4810.
(40) Wang, L.; He, X.; Sun, W.; Wang, J.; Li, Y.; Fan, S. *Nano Lett.* **2012**, *12* (11), 5632−5636.
(41) Ramana, C. V.; Mauger, A.; Gendron, F.; Julien, C. M.; Zaghib, K. *J. Power Sources* **2009**, *187* (2), 555−564.
(42) Zhu, T.; Li, J. *Prog. Mater. Sci.* **2010**, *55* (7), 710−757.
(43) Tolbert, S. H.; Alivisatos, A. P. *Annu. Rev. Phys. Chem.* **1995**, *46* (1), 595−626.
(44) Lerotic, M.; Jacobsen, C.; Gillow, J. B.; Francis, A. J.; Wirick, S.; Vogt, S.; Maser, J. *J. Electron Spectrosc. Relat. Phenom.* **2005**, *144*−*147*, 1137−1143.
(45) Liu, Y.; Meirer, F.; Williams, P. A.; Wang, J.; Andrews, J. C.; Pianetta, P. *J. Synchrotron Rad.* **2012**, *19* (2), 281−287.
(46) Wagemaker, M.; Singh, D. P.; Borghols, W. J. H.; Lafont, U.; Haverkate, L.; Peterson, V. K.; Mulder, F. M. *J. Am. Chem. Soc.* **2011**, *133* (26), 10222−10228.
(47) Cogswell, D. A.; Bazant, M. Z. *ACS Nano* **2012**, *6* (3), 2215−2225.
(48) Andersson, A. S.; Thomas, J. O. *J. Power Sources* **2001**, *97*−*98*, 498−502.
(49) Saravanan, K.; Balaya, P.; Reddy, M. V.; Chowdari, B. V. R.; Vittal, J. J. *Energy Environ. Sci.* **2010**, *3* (4), 457−463.
(50) Liu, J.; Kunz, M.; Chen, K.; Tamura, N.; Richardson, T. J. *J. Phys. Chem. Lett.* **2010**, *1* (14), 2120−2123.
(51) Wagemaker, M.; Borghols, W. J. H.; Mulder, F. M. *J. Am. Chem. Soc.* **2007**, *129* (14), 4323−4327.
(52) Lucas, I.; McLeod, A.; Syzdek, J.; Middlemiss, D. S.; Grey, C. P.; Basov, D. N.; Kostecki, R. M. *Nano Lett.* **2015**, *15* (1), 1−7.
(53) Wang, D.; Wu, X.; Wang, Z.; Chen, L. *J. Power Sources* **2005**, *140* (1), 125−128.
(54) McDowell, M. T.; Lee, S. W.; Nix, W. D.; Cui, Y. *Adv. Mater.* **2013**, *25* (36), 4966−4985.
(55) Song, H.-K.; Lee, K. T.; Kim, M. G.; Nazar, L. F.; Cho, J. *Adv. Funct. Mater.* **2010**, *20* (22), 3818−3834.
(56) Woodford, W. H.; Chiang, Y.-M.; Carter, W. C. *J. Electrochem. Soc.* **2010**, *157* (10), A1052−A1059.

DOI: 10.1021/acs.nanolett.5b01314
Nano Lett. XXXX, XXX, XXX−XXX